


Electrocatalysis Very Important Paper

 How to cite: *Angew. Chem. Int. Ed.* **2025**, 64, e202500546
 doi.org/10.1002/anie.202500546

Interfacial Lithium Cations Catalyze Biomimetic Aerobic Oxygenation via Short-Range Electrostatic Interaction

 Shuangshuang Cha⁺, Yizhou Yang⁺, Wei Du, Tao Jiang, Ran Wang, Mengxin Qu, Zhe Ji, Chang Yan, Xuejing Yang,^{*} and Ming Gong^{*}

Abstract: Enzymes often involve short-range electrostatic interactions in the deliberate microenvironment for accelerating the catalysis. Comparatively, electrostatic interactions from ions in solutions are mostly shielded by solvent or counterion shells, creating negligible catalytic effects. Herein, we discovered that the interfacial Li⁺ cations accumulated on electrodes catalyze the selective water-involved O₂ electro-reduction into peroxide anion (OOH⁻), forming an active side-on Li⁺-OOH⁻ complex via short-range electrostatic interaction. This complex reduces the O₂ reduction energy barrier and increases the nucleophilicity, expediting the aerobic oxygenation of ketones. Aside from trapping active intermediates, Li⁺ cations also attract the excessive water dipoles to prevent them from quenching the active Li⁺-OOH⁻ complex. By using probe-assisted quantitative methods, we demonstrated the unique under-coordinative characteristics of interfacial Li⁺ for interacting with reaction intermediates, and the effective concentration of under-coordinative Li⁺ on the interface is an order of magnitude higher than in the bulk solution. These analyses provide essential evidences about the intrinsic difference between bulk ions and interfacial ions toward catalysis.

Introduction

Short-range electrostatic interactions are ubiquitous in catalytic systems and play decisive roles in catalytic activity and stereoselectivity.^[1-4] The electrostatic attraction between the positively charged and negatively charged centers from ions, dipoles, or polar functional groups modulates the configurations and energies of the reactants or intermediates, steering toward the targeted reaction pathway.^[5-8] These

electrostatic interactions are also the selection of nature and drive almost all molecular processes in biological systems, including protein folding, molecular recognition, and enzyme catalysis.^[9-11] Specifically, the charged centers in enzymes precisely position the key intermediates toward tremendous rate acceleration and superior selectivity.^[12,13]

Taking Baeyer Villiger monooxygenase (BVMO) as an example, electrostatic interactions enable the efficient oxygenation of ketones into the corresponding esters using O₂ as the only oxidant, avoiding the use of unstable peracids in conventional processes.^[14-18] The catalytic process of BVMO reduces flavin that binds O₂ to form the reactive charged center.^[17] Meanwhile, the NADP⁺ amide establishes a crucial electrostatic interaction with the hydrogen on the flavin's N5 site, which prevents the internal proton transfer to form the undesired hydrogen peroxide. The charged amino residues of the protein scaffold also position the ketone substrate to expedite the nucleophilic attack of the peroxy anion center.^[19,20] Inspired by these natural enzymes, researchers have been dedicated to mimicking the enzymes by creating highly stereoscopic 3D structures. However, these structures are rather rigid compared to the dynamic and flexible enzyme active centers dominated by weak interactions. In contrast, the electrostatic forces on the electrode/electrolyte interface spontaneously form the double-layer structure that features an open, highly dynamic environment prioritized by weak interactions. This can potentially mimic the enzymatic environment for creating the desired chemo-reactivity but still remains challenging.^[4,21-25]

Herein, we discover that the Li⁺ cations at the electrode/electrolyte interface can act as catalytic centers toward biomimetic aerobic oxygenation of ketones (Scheme 1). Bulk cations in solution are often surrounded by dipoles (e.g., H₂O

[*] S. Cha⁺, W. Du, T. Jiang, R. Wang, M. Qu, M. Gong
 Department of Chemistry and Shanghai Key Laboratory of Molecular Catalysis and Innovative Materials, Fudan University, Shanghai 200438, P.R. China
 E-mail: gongm@fudan.edu.cn

Y. Yang⁺, X. Yang
 National Engineering Laboratory for Industrial Wastewater Treatment, East China University of Science and Technology, Shanghai 200237, P.R. China
 E-mail: xj.yang@ecust.edu.cn

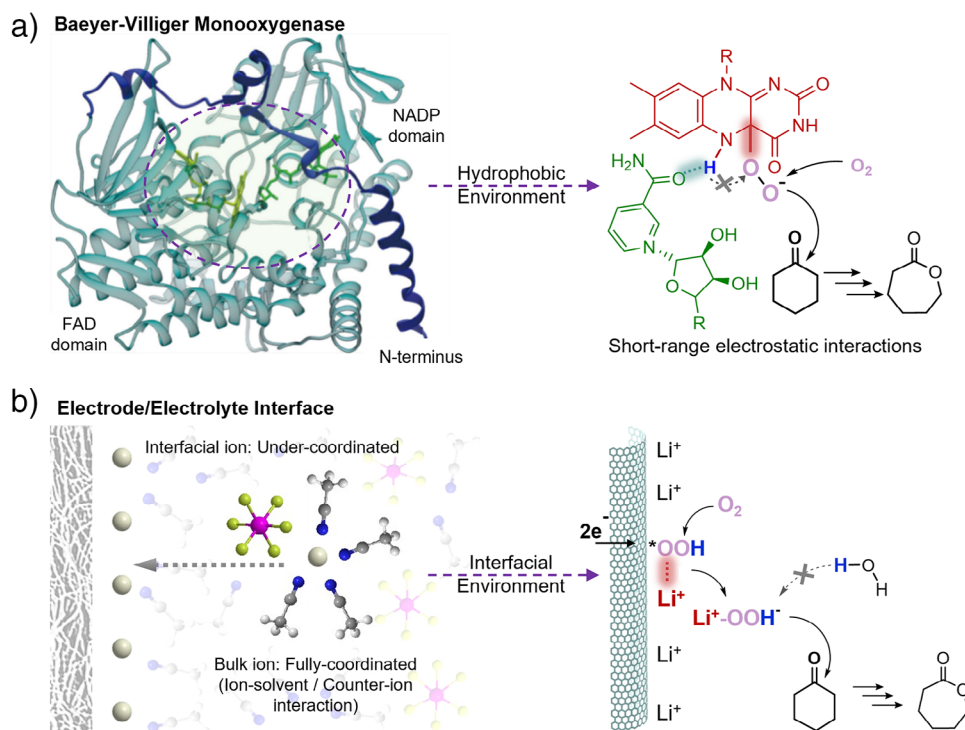
Z. Ji
 College of Chemistry and Molecular Engineering, Peking University, Beijing 100871, P.R. China

C. Yan
 Center for Ultrafast Science and Technology, School of Chemistry and Chemical Engineering, Shanghai Jiao Tong University, Shanghai 200240, P.R. China

C. Yan
 Zhangjiang Institute for Advanced Study, Shanghai Jiao Tong University, Shanghai 200240, P.R. China

[⁺] Both authors contributed equally to this work.

Additional supporting information can be found online in the Supporting Information section



Scheme 1. Schematic illustration of enzymatic and biomimetic aerobic oxygenation. a) The mechanism of BVMO enzyme.^[17] b) Biomimetic mechanism of aerobic oxygenation by electrostatically enriched Li^+ .

in aqueous systems) or counter-ions (e.g., anions in nonpolar solvents) via strong electrostatic interactions, which prevents the formation of desired electrostatic interactions with target substrates or intermediates. Therefore, these cations had been considered as bystanders or helpers and seldom regarded as the catalytic centers,^[26–28] but the interfacial cations on electrodes could create a unique microenvironment toward the desired electrostatic interactions that perform catalysis.^[29] In this system, the Li^+ cations with under-coordinated characteristics can form short-range electrostatic interactions with the in situ formed oxygen species from O_2 reduction. Due to the minimal H_2O content in the acetonitrile-based electrolyte, Li^+ cations replace protons during the electron transfer processes, selectively forming an active $\text{Li}^+ \text{--} \text{OOH}^-$ complex that encourages the nucleophilic attack to ketones for oxygenation. This route of O_2 -driven oxygenation provides an alternative way to the conventional electro-oxidation systems that use water or peroxide as the oxygen source.^[30,31]

Results and Discussion

Interfacial Li^+ Cations Promote the Aerobic Electrochemical Oxygenation of Ketones

The aerobic electrochemical oxygenation of ketones resembles the BVMO process and demands the selective O_2 reduction into the reactive oxygen species, which then catalyzes the sequential oxygenation (e.g. cyclohexanone to ϵ -

caprolactone (ϵ -CL)). We first screened different cations and discovered a dramatic difference among their electrocatalytic performances (Figure 1a). In organic electrosynthesis systems, tetraalkylammonium salts (e.g. tetrabutylammonium (TBA)) are typically used to ensure sufficient solubility and ionic conductivity. However, the TBA cations can only produce an ϵ -CL yield of 8.1% with a Faradaic efficiency of 13.0%. Shrinking the sizes of the ammonium cations can slightly improve the yield but only to <15.0%. Interestingly, 0.1 M Li^+ cations tremendously improved the ϵ -CL yield to 41.7% with a Faradaic efficiency of 67.1%, much superior to TBA^+ . Other alkali metal cations (e.g. Na^+/K^+) showed some promotional effects but exhibited inferior yields of ϵ -CL yield due to their larger ionic radii (Figure S1).

Electrode material is another seminal component of the electrochemical system. Under the identical 0.1 M Li^+ , carbon-based electrodes that favor the two-electron O_2 reduction outperformed the Pt/C electrode that encourages the four-electron O_2 reduction, suggesting the necessity of in situ formed reactive oxygen species.^[32–35] Various carbon-based electrodes exhibited similar performance, with the slightly higher ϵ -CL yield on the carboxylated multi-walled carbon nanotubes (CNT-COOH), likely originating from the negatively charged carboxylate that encourages the accumulation of interfacial Li^+ cations (Figure S2). Accordingly, CNT-COOH was utilized as the cathode with Pt as the anode, and Li^+ and TBA⁺ were utilized as representative cations in the following study. The effect of the Pt anode was excluded by showing comparable performance on the fluorine-doped tin oxide (FTO) anode (Figure S3).

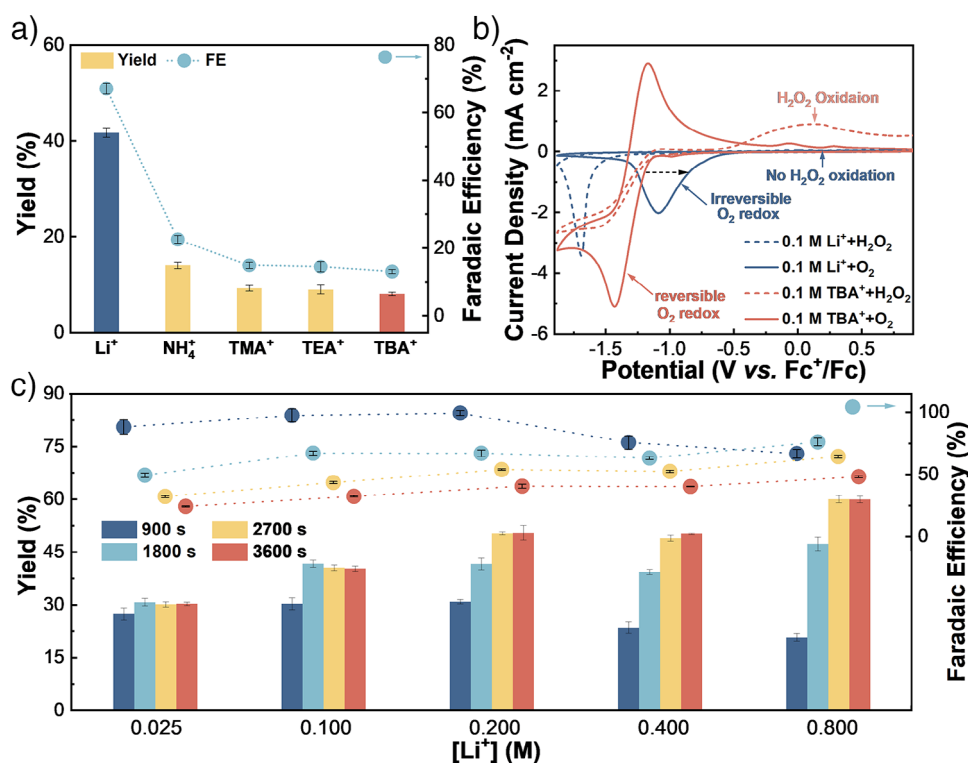


Figure 1. Interfacial Li cations promote the aerobic electrochemical oxygenation of ketones. a) The yield/Faradaic efficiency of ϵ -CL with different cations. Electrolysis conditions: 60 mM cyclohexanone, 0.1 M salts, 5 mL acetonitrile, room temperature, constant current density of 20 mA cm^{-2} for 2700 s. b) Cyclic voltammograms of $\text{O}_2/\text{H}_2\text{O}_2$ reduction under Li^+ or TBA^+ on a glassy carbon electrode. The scan rate is 100 mV s^{-1} . c) Time-dependent ϵ -CL yield/Faradaic efficiency under different concentrations of LiPF_6 . Electrolysis conditions: 60 mM cyclohexanone, 0.025/0.1/0.2/0.4/0.8 M LiPF_6 , 5 mL acetonitrile, room temperature, constant current density of 20 mA cm^{-2} for 900/1800/2700/3600 s. The error bars correspond to the standard deviation of at least three independent measurements, and the center value for the error bars is the average of the three independent measurements.

According to the cyclic voltammetry (CV), the kinetics was greatly expedited with the positively shifted onset potential of O_2 reduction from -1.12 V versus Fc^+/Fc under TBA^+ to -0.55 V versus Fc^+/Fc under Li^+ (Figure 1b), demonstrating catalytic behaviors. In stark contrast to a pair of reversible single-electron O_2/O_2^- redox pair^[36] that is sensitive to proton sources under TBA^+ system (Figure S4), the Li^+ system showed the irreversible O_2 reduction and the absence of oxidation current until $\sim 1.0 \text{ V}$ versus Fc^+/Fc (Figure S5). This suggests the formation of a robust complex upon Li^+ interaction, likely the anionic species generated from O_2 reduction.

The simplest method of enhancing the Li^+ -mediated interactions is to increase the Li^+ concentrations. This enhanced interaction led to an improved ϵ -CL yield to 60.1% under 0.8 M Li^+ that approaches saturation (Figure 1c, S6, and S7). The time-dependent product analysis revealed that the reactions were mostly completed in 2700 s, and the general trend followed the higher yield and Faradaic efficiency under a higher Li^+ concentration. The Faradaic efficiency under a moderate Li^+ concentration of 0.2 M under 900 s could even reach 99.4%, while this value gradually diminishes over prolonging the electrolysis due to the consumed reactants for the insufficient consumption of O_2 -reduction products.

Properties of Short-Range $\text{Li}^+ - \text{OOH}^-$ Interactions

We first gleaned the active species generated from the Li^+ -mediated O_2 reduction. According to the cationic nature of Li^+ , three possible active species were considered: Li superoxide (LiO_2), Li peroxide (Li_2O_2), and Li peroxide anion complex ($\text{Li}^+ - \text{OOH}^-$). The former two species have often been observed in the organic-phase $\text{Li} - \text{O}_2$ batteries,^[37–39] while the introduction of water (H_2O) can form the latter species. Consequently, we first investigated the H_2O dependence on the catalytic activity of O_2 -driven oxygenation. It is worthwhile to note that the acetonitrile solvent and constant O_2 purging in the open-air system inevitably introduces H_2O into the reaction. Even though these trace amounts of H_2O are not sufficient as the oxygen source for the anodic ketone oxidation, they can serve as the proton source toward the formation of $\text{Li}^+ - \text{OOH}^-$ (Figure S8). To minimize the H_2O content, we used dry acetonitrile and compared the performance at shorter durations (Figure S9). Obviously, reducing the H_2O content significantly decreased the yields and Faradaic efficiencies of the desired ϵ -CL, which reached the plateau beyond a H_2O content of $\sim 0.1 \text{ M}$. Further reducing the electrolysis duration to minimize the H_2O content introduced by O_2 purging in the dry system eliminated the product, while obvious product was resolved

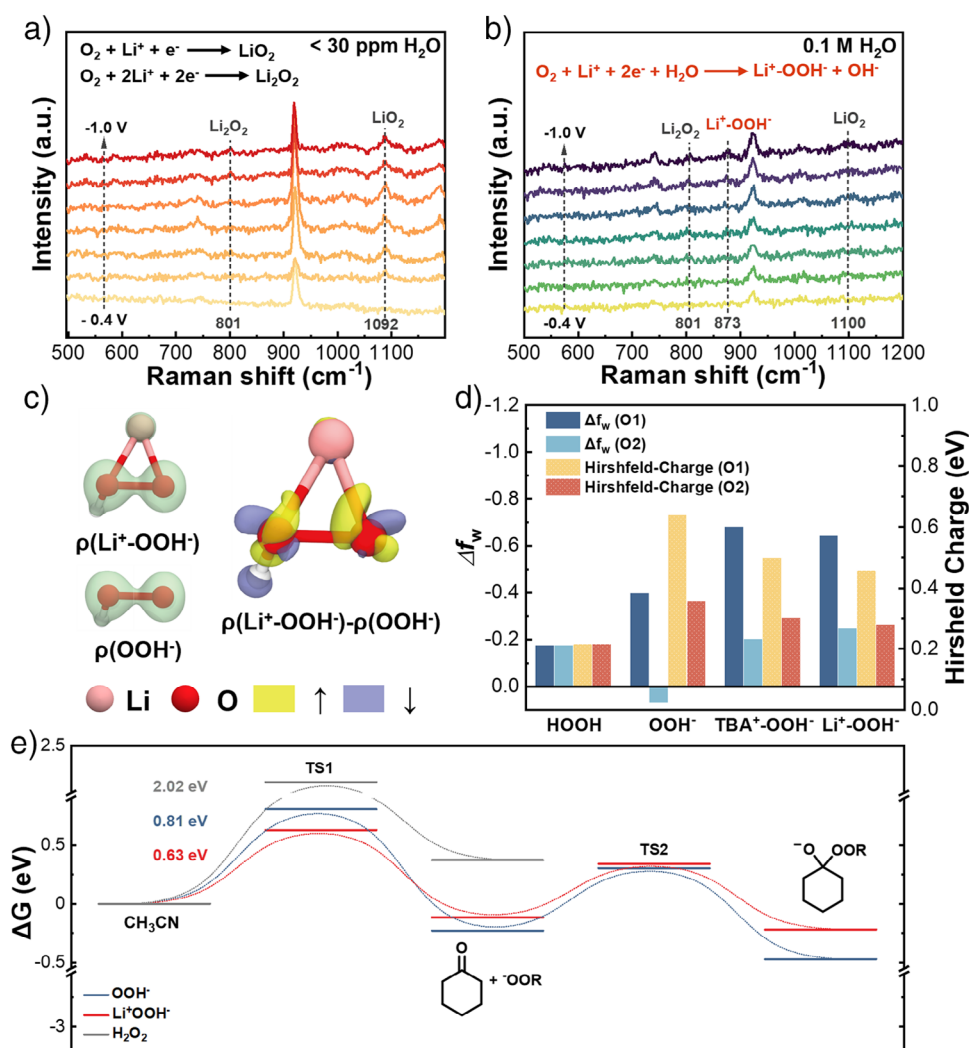


Figure 2. The origin and properties of the short-range $\text{Li}^+\text{-OOH}^-$ electrostatic interaction. a) and b) The in situ SERS spectra of the acetonitrile/dry acetonitrile system when polarized to different potentials in an electrolyte with Li^+ under O_2 . c) Calculated electron density and their difference of $\text{Li}^+\text{-OOH}^-$ complex and OOH^- anion (value = 0.007 a.u.; blue represents a decrease in the electron density, yellow represents the opposite). d) The electrophilicity of each oxygen atom on H_2O_2 and OOH^- with/without cationic coordination described by orbital weighted Fukui functions and condensed duality descriptors (O1 represents the O atom away from the H and O2 represents the O atom close to the H). e) The Gibbs free energy distribution of the cyclohexanone oxygenation pathway (to Criegee adduct).

in the wet system (Figure S10). This illustrates the essential role of H_2O in forming the active complex, which likely leans toward the $\text{Li}^+\text{-OOH}^-$ complex.

We then carried out the in situ surface-enhanced Raman spectroscopy (SERS) analysis (Figure 2a,b). In the dry acetonitrile system with a H_2O content of $< 30 \text{ ppm}$, we resolved the evolution of Li_2O_2 and LiO_2 at 801 and 1092 cm^{-1} beyond -0.5 V versus Fc/Fc^+ , similar to the studies on the Li-O_2 battery. However, dosing 0.1 M H_2O into the system diminished the signals from these species and also generated an additional band at 873 cm^{-1} beyond -0.8 V versus Fc/Fc^+ , likely originating from the $\text{Li}^+\text{-OOH}^-$ complex. This complex was also evidenced by its slight redshift from the H_2O_2 counterpart (Figure S11). The absence of $\text{Li}^+\text{-OOH}^-$ Raman band and significantly lower oxygenation activity under H_2O -less systems indicate the possible active species of $\text{Li}^+\text{-OOH}^-$ ion pair.

This $\text{Li}^+\text{-OOH}^-$ short-range electrostatic interaction was further confirmed by the negatively shifted peaks under O_2 -free and H_2O_2 conditions in the Li^+ system as well as the disappearance of the H_2O_2 oxidation on the reversed scan compared to the TBA^+ system (Figure 1b). This H_2O_2 oxidation wave was highly dependent on the Li^+ concentrations, with obvious peaks under 0.025 M Li^+ and its absence beyond 0.1 M Li^+ , indicating the more effective $\text{Li}^+\text{-OOH}^-$ interaction under higher Li^+ concentrations (Figure S12).

The ultraviolet-visible (UV-vis) spectra of the cyclohexanone-free catholyte further confirmed the $\text{Li}^+\text{-OOH}^-$ complex from the broad peak that emerged at 273.3 nm that shifted under different Li^+ concentrations (Figures S13 and S14).^[40] After its accumulation, adding cyclohexanone with a 15-min reaction without applied potential could produce $\epsilon\text{-CL}$ (Figure S15), while no product could be detected without this accumulation (Figure S16),

further demonstrating the active $\text{Li}^+\text{-OOH}^-$ oxidant. The configuration of the $\text{Li}^+\text{-OOH}^-$ complex is key to its reactivity. Intuitively, the OOH^- anion should be more nucleophilic toward attacking ketones, while the formation of $\text{Li}^+\text{-OOH}^-$ should quench its nucleophilicity like H_2O_2 . Thus, we calculated the most thermodynamically stable configuration of the $\text{Li}^+\text{-OOH}^-$ complex as a side-on form with the three-center bonding (Figure 2c).

We further investigated the chemical property of this side-on $\text{Li}^+\text{-OOH}^-$ complex by calculating the electrophilicity of each oxygen atom, using the orbital-weighted Fukui functions and condensed dual descriptor (Δf_w).^[41] (Figure 2d). The formation of the cation- OOH^- interactions drastically decreases the Δf_w values compared to bare OOH^- , corresponding to the increased nucleophilicity that benefits the oxygenation process. Additionally, the calculated Hirshfeld charges reveal the significantly decreased Lewis basicity from OOH^- to $\text{TBA}^+\text{-OOH}^-$ and further to $\text{Li}^+\text{-OOH}^-$. The diminished Lewis basicity enhanced the structural stability of the $\text{Li}^+\text{-OOH}^-$ complex to prevent its protonation and form the much less active H_2O_2 . These results could be explained by the changes in the electron density surrounding the terminal O atom (Figure 2c). The depletion of electron density away from the plane decreases the tendency of H_2O_2 formation, since this direction is consistent with the more stable bent form of H_2O_2 , whereas, the increased electron density away from the Li^+ can still contribute to the enhanced nucleophilicity.

Nevertheless, the similarly calculated properties of $\text{Li}^+\text{-OOH}^-$ and $\text{TBA}^+\text{-OOH}^-$ complexes could not explain the drastic reactivity differences observed. This suggested that Li^+ not only affects the formation of $\text{Li}^+\text{-OOH}^-$ complex but also influences the O_2 reduction pathway. Previous studies have revealed that, due to the strong electrostatic interactions,^[28,42] Li^+ can impact the O_2 reduction pathway by promoting an outer-sphere (OS) electron transfer pathway toward H_2O_2 formation in an aqueous electrolyte. Similar electrostatic interactions exist in our system for governing the O_2 reduction pathway, but our acetonitrile-based electrolyte with minimal H_2O content leads to much weaker $\text{Li}^+\text{-solvent}$ interactions that facilitate the accumulation of under-coordinative Li^+ on the electrode/electrolyte interface. The proton in the -COOH group on the CNT could also be substituted by Li^+ to maximize the local accumulation of Li^+ . These Li^+ cations with smaller solvent shells can penetrate the double layer for promoting the inner-sphere (IS) electron transfer pathway. Meanwhile, due to the existence of defective sites in the CNT-COOH catalyst, the in situ formed oxygen species, such as $^*\text{OOH}$, have relatively strong adsorption capabilities toward reduction via the IS pathway. The interfacial Li^+ would then exert its strong electrostatic interactions on the $^*\text{OOH}$ species, which reduces the kinetic barrier of $\text{Li}^+\text{-OOH}^-$ formation (Figures S17–S19). Comparatively, the bulky and hydrophobic nature of TBA^+ can hardly cause its compact accumulation at the interface but exclude the H_2O molecules required for the OOH^- formation. Ab initio metadynamics MD simulation also confirmed the higher dissociation free energy of $\text{Li}^+\text{-OOH}^-$ than $\text{TBA}^+\text{-OOH}^-$ in the acetonitrile solution (Figure S20) for more favorable

$\text{Li}^+\text{-OOH}^-$ formation. These calculated results explain the observed reversible O_2 redox under TBA^+ but irreversible O_2 redox under Li^+ toward $\text{Li}^+\text{-OOH}^-$ complex formation (Figure 1b), likely facilitating the accumulation of Li^+ in the inner sphere.

The determination of this active species helps elucidate the molecular-level oxygenation mechanism (Figures 2e and S21). Like other oxygenation systems, acetonitrile is a crucial mediator and creates a reactive adduct with a more favorable leaving group (Figure S22). Thus, the $\text{Li}^+\text{-OOH}^-$ complex first nucleophilically attacks the acetonitrile to form the peroxyacetonitrile adduct (OOR^-), which can still form the short-range Li^+ interactions by $\text{Li}^+\text{-OOR}^-$. This complex can effectively attack the cyclohexanone to form a Criegee adduct, which further undergoes typical rearrangement to generate $\epsilon\text{-CL}$ and acetamide (Figures S23 and S24).

Competition Between $\text{Li}^+\text{-OOH}^-$ Interaction and Solvation/ $\text{Li}^+\text{-Anion Attraction}$

Under 0.1 M Li^+ , the absence of the H_2O_2 oxidation wave in the CV curve clearly indicated the $\text{Li}^+\text{-OOH}^-$ interaction, but no product was detected using H_2O_2 as the oxidant without applied potential. Due to the interfacial electric field and incomplete dissociation of the salt, the bulk Li^+ concentration is not an effective indicator of its ability to form the $\text{Li}^+\text{-OOH}^-$ complex as well as the local Li^+ concentration at the interface. Consequently, we define the fractional concentration of Li^+ capable of forming $\text{Li}^+\text{-OOH}^-$ complexes as the effective Li^+ concentration. The key factors that affect the effective Li^+ concentration are the species that can competitively coordinate to the Li^+ , mainly including H_2O and counter-ion.

H_2O has been proven to be effective in the formation of $\text{Li}^+\text{-OOH}^-$ complex as the proton donor for the O_2 reduction. In the above study, H_2O was minimally introduced as reactants, but in fact the excessive H_2O molecules can donate their dissociated protons to quench the active $\text{Li}^+\text{-OOH}^-$ complex. Therefore, we additionally introduced H_2O into the system to examine the dependence of Li^+ on the oxygenation activity, and the detailed H_2O contents were estimated by NMR (Figure S25). Comparing the polarization curves under different H_2O contents demonstrated a distinct positive potential shift (Figure 3a). Dosing beyond 5% H_2O led to the decreasing current at the first stage but the much-elevated current for deep O_2 reduction at approx. -0.9 V versus Fc^+/Fc . Therefore, H_2O can be a double-edged sword that simultaneously benefits the O_2 reduction kinetics and destroys the desired $\text{Li}^+\text{-OOH}^-$ complex to encourage deep reduction. Under 0.8 M Li^+ , the positive shift was still present, but the change at 5% H_2O disappeared, suggesting the enhanced H_2O tolerance (Figure 3b). Accordingly, under 0.1 M Li^+ , the $\epsilon\text{-CL}$ yield decreased from 41.2% of 0% H_2O to 21.7% of 1% H_2O , while under 0.8 M Li^+ , the $\epsilon\text{-CL}$ yield was almost maintained, and only the excessive H_2O dosage led to further decreased yield (Figure 3c). The time-dependent product analysis with different H_2O contents

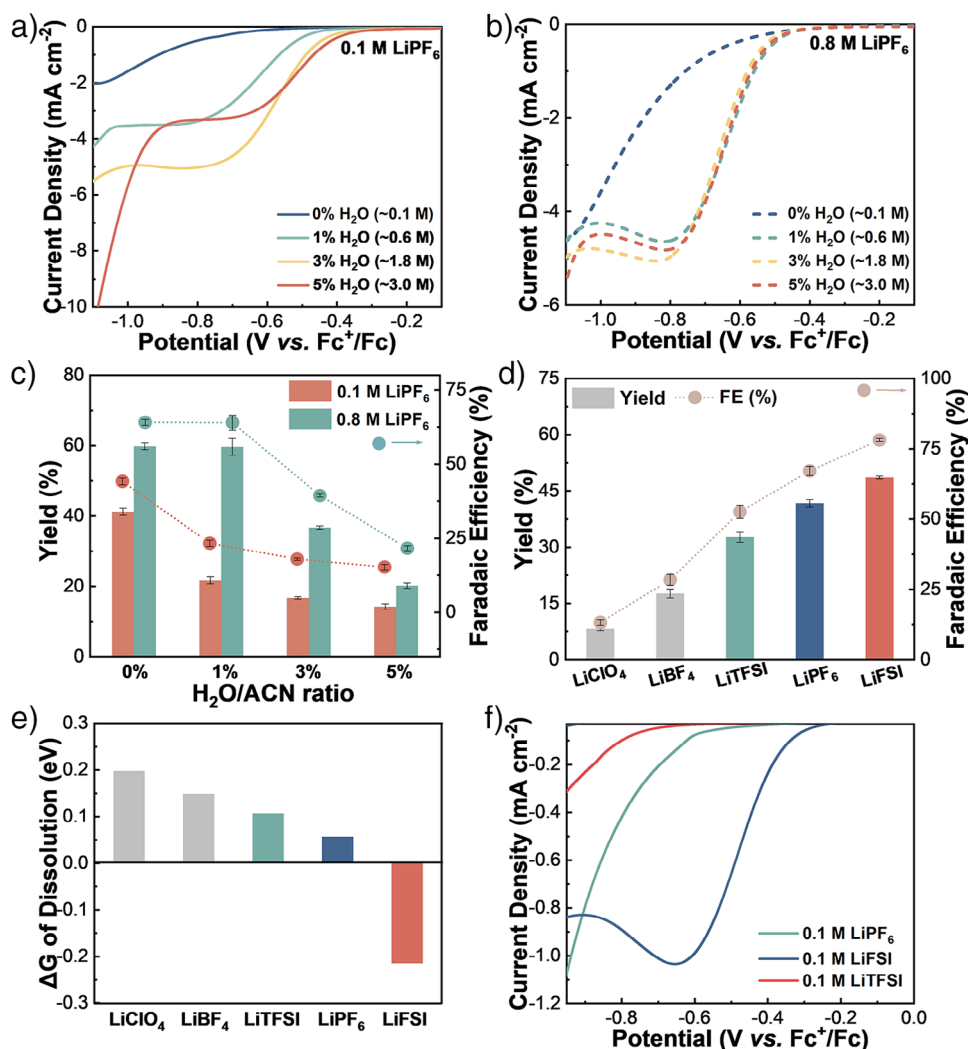
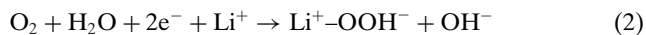
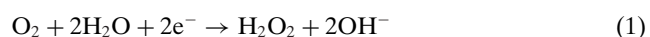


Figure 3. Competition between $\text{Li}^+\text{-OOH}^-$ interaction and $\text{Li}^+\text{-solvent/Li}^+\text{-anion}$ interaction. a and b) Polarization curves of O_2 reduction in a) 0.1 M and b) 0.8 M LiPF_6 system with different H_2O contents. c) The yield and Faradaic efficiency of $\varepsilon\text{-CL}$ in 0.1/0.8 M LiPF_6 system with different H_2O contents. Electrolysis conditions: 60 mM cyclohexanone, 0.1/0.8 M LiPF_6 , 0%/1%/3%/5% H_2O , 5 mL acetonitrile, room temperature, constant current density of 20 mA cm^{-2} for 2700 s. d) The yield and Faradaic efficiency of $\varepsilon\text{-CL}$ in Li salt systems with different anions. Electrolysis conditions: 60 mM cyclohexanone, 0.1 M salts, 5 mL acetonitrile, room temperature, constant current density of 20 mA cm^{-2} for 2700 s. e) Calculated Gibbs energies of dissolution for Li salts with different anions. f) Polarization curves of O_2 reduction under Li salts with different anions. The error bars correspond to the standard deviation of at least three independent measurements, and the center value for the error bars is the average of the three independent measurements.

further confirmed the H_2O effect and H_2O -tolerance of 0.8 M Li^+ (Figure S26). Under 900 s, dosing 1% H_2O increased the yield with a much-improved Faradaic efficiency to 99.6%.

To further verify the Li^+/H^+ competition of the H_2O effect, we utilized the rotating ring disk electrode (RRDE) to measure the kinetics influenced by the reaction microenvironment. Theoretically, the reduction of O_2 to H_2O_2 or OOH^- involves the generation of 1 OH^- per e^- through a conventional proton-coupled electron transfer (PCET) process (Equation 1). However, the reduction of O_2 to $\text{Li}^+\text{-OOH}^-$ with the H^+/Li^+ competition generates only one OH^- but transfers two electrons (Equation 2), which could lead to a different interfacial pH gradient.



We cathodically biased the ring electrode to the hydrogen evolution potentials and measured the kinetics differences with and without the O_2 reduction on the disk electrode. The larger current difference corresponds to the larger proton gradient. By comparing the scenarios of 0% and 5% H_2O , we discovered that a higher H_2O content exhibited a much higher current difference and a faster current response (Figure S27), corresponding to a higher pH gradient approaching the Equation 1 scenario with a strong protonation tendency.

Counterion is another central factor that governs the effective Li^+ concentration. In nonaqueous systems with low dielectric constants, $\text{Li}^+\text{-anion}$ interaction can universally occur in solutions to compete with OOH^- .^[43,44]

The oxygenation activity trend followed the order of $\text{LiClO}_4 < \text{LiBF}_4 < \text{LiTFSI} < \text{LiPF}_6 < \text{LiFSI}$ (Figure 3d), which is in coincidence with the calculated trend of the free energy of dissociation for different salts (Figure 3e). The stronger Li–anion interaction leads to the higher competition and lower tendency to form the $\text{Li}^+ \text{--} \text{OOH}^-$ complex. The O_2 reduction onset potential also exhibited a consistent trend, clearly indicating a promotion effect of the dissociated Li^+ (Figure 3f). LiFSI can be spontaneously dissociated in acetonitrile and produces the highest ε -CL yield of 48.6% under 0.1 M.

In all, the effective Li^+ cations can serve as two major roles: 1) The under-coordinated Li^+ can effectively trap the in situ generated OOH^- species to form the reactive side-on $\text{Li}^+ \text{--} \text{OOH}^-$ complex that mimics the active center of the BVMOs; 2) The excessive Li^+ dissociated from the salt can form the Li^+ –dipole interaction with H_2O that prevents the protonation to destruct the $\text{Li}^+ \text{--} \text{OOH}^-$ complex, which acts as an analogy to the electrostatic interaction of the NADPH cofactor that prevents H_2O_2 formation (Scheme 1). These Li^+ cations functionally mimic the enzymes via weak interactions toward high oxygenation activity, but the electrode/electrolyte interface is still considered a more open and dynamic environment than the enzyme pocket, which needs further modulation toward maximizing the desired interaction toward enzyme-like chemoselectivity.

Quantitative Description of Interfacial Li^+ Cations

Since the accumulated Li^+ cations possess a much higher concentration at the interface than the bulk electrolyte, this difference in the effective Li^+ concentration might be a key contributor to the observed oxygenation activity as well as the activity difference between electrocatalysis and thermocatalysis (Figure 4a). Therefore, we aimed to quantify this effective Li^+ concentration both at the interface and in the bulk. To mimic the bulk electrolyte scenario, we added H_2O_2 as the oxidant, and Li^+ -driven H_2O_2 dissociation into $\text{Li}^+ \text{--} \text{OOH}^-$ formed the active species. The addition of 0.025 and 0.1 M LiPF_6 generated no ε -CL product and failed to compete with H^+ corresponding to a low effective Li^+ concentration (Figure 4b). Increasing the cyclohexanone concentration also demonstrated no ε -CL product, suggesting the limited oxidant for driving the reaction (Figure S28). This also indicates that Li^+ is less likely to act as Lewis acid alone for activating the ketone, like other Lewis acid-driven oxygenation systems. Comparatively, modest yields of ε -CL could be obtained under the interfacial Li^+ . We only observed ε -CL production under H_2O_2 beyond 0.2 M Li^+ . Interestingly, the ε -CL yield under H_2O_2 with 0.8 M Li^+ was almost equivalent to that under electrochemical O_2 reduction with 0.1 M Li^+ . It might indicate that assuming similar microenvironments near the vicinity of Li^+ , the concentration of interfacial cations is approx. eight times higher than the bulk concentration.

However, the direct quantification of the effective Li^+ still remains to be solved. Since the spectroscopic signal of the $\text{Li}^+ \text{--} \text{OOH}^-$ is not well-defined and affected by solvent

species, we utilized an azide (N_3^-) probe to mimic the OOH^- anion. The infrared N_3^- vibrations have well-defined peaks with negligible background interference, and the short-range $\text{Li}^+ \text{--} \text{N}_3^-$ interaction could also cause a shift in the N_3^- vibrational peak, allowing for the quantification of their relative abundance. The SEIRAS spectra in 0.1 M Li^+ at -0.5 V versus Fc^+/Fc near open-circuit potential (OCP) resembles the thermocatalytic condition. Two major vibration peaks of ~ 2110 cm^{-1} from the $\text{Li}^+ \text{--} \text{N}_3^-$ and ~ 2080 cm^{-1} from the solvated N_3^- appeared at this potential (Figures 4c and S29). After applying -1.5 V versus Fc^+/Fc , an additional peak at 2148 cm^{-1} emerged, corresponding to the N_3^- coordinated to multiple Li^+ ($\text{nLi}^+ \text{--} \text{N}_3^-$). This likely originated from the relatively low solubility of LiN_3 solid and high Li^+ to N_3^- ratio used (0.1 M Li^+ versus <0.01 M N_3^-). Under 0.8 M Li^+ , an apparent peak at 2180 cm^{-1} was observed even at OCP, and this more blueshifted peak was likely attributed to the LiN_3 crystallites that contain the multiple $\text{Li}^+ \text{--} \text{N}_3^-$ coordination. Biasing the system to -1.5 V versus Fc^+/Fc recovered to three major peaks at 2147, 2104, and 2078 cm^{-1} (Figure 4d). The well-defined peak shapes allowed the quantification of the relative proportions of these species near OCP that represents the bulk electrolyte under thermocatalytic conditions and -1.5 V versus Fc^+/Fc that represents the interface under electrocatalytic conditions (Figure 4e,f). Under thermocatalytic conditions, the major component is the solvated N_3^- with negligible contribution of $\text{nLi}^+ \text{--} \text{N}_3^-$, while extending beyond 0.2 M Li^+ significantly increased the proportions of $\text{nLi}^+ \text{--} \text{N}_3^-$ and $\text{Li}^+ \text{--} \text{N}_3^-$. Under 0.8 M Li^+ , the relative proportion of $\text{nLi}^+ \text{--} \text{N}_3^-$ could reach 17.35%. Under electrocatalytic conditions, a significant proportion of 16.12% for $\text{nLi}^+ \text{--} \text{N}_3^-$ was present even in 0.1 M Li^+ , which further increased to 38.6% under 0.8 M Li^+ .

We then used the Kendall correlation coefficient to illustrate the relevance of this quantification with B-V oxygenation activity (Figure 4g,h). The correlation coefficient based on the proportion of $\text{nLi}^+ \text{--} \text{N}_3^-$ was the highest among all three species, and further including the $\text{Li}^+ \text{--} \text{N}_3^-$ did not benefit the coefficient, suggesting the central species of $\text{nLi}^+ \text{--} \text{N}_3^-$. It is worthwhile to emphasize that the relative solubility differences between LiN_3 and LiOOH may give rise to the difference in the coordination environment of Li^+ to N_3^- and OOH^- , but this correlation still raises attention to the possible active anionic species coordinated to multiple cations due to the highly concentrated cations at the electrode interface. Another important evidence is that the proportion of $\text{nLi}^+ \text{--} \text{N}_3^-$ under 0.8 M Li^+ and thermocatalytic conditions is 17.35%, very close to the 16.12% under 0.1 M Li^+ and electrocatalytic conditions. This was highly consistent with the trend of the ε -CL yield, indicating that we might successfully quantify the effective Li^+ concentration via the N_3^- -assisted method. Under 0.1 M bulk concentration, no effective Li^+ with undercoordination characteristics could be obtained in the bulk, while the effective ratio could reach $\sim 20\%$ at the interface, while this value could only be achieved for the bulk by occupying the Li^+ concentration.

The differences in the thermocatalytic and electrocatalytic systems could be extended to other Li^+ salts, such as LiFSI and LiTFSI (Figures S30 and S31). Both anions showed the

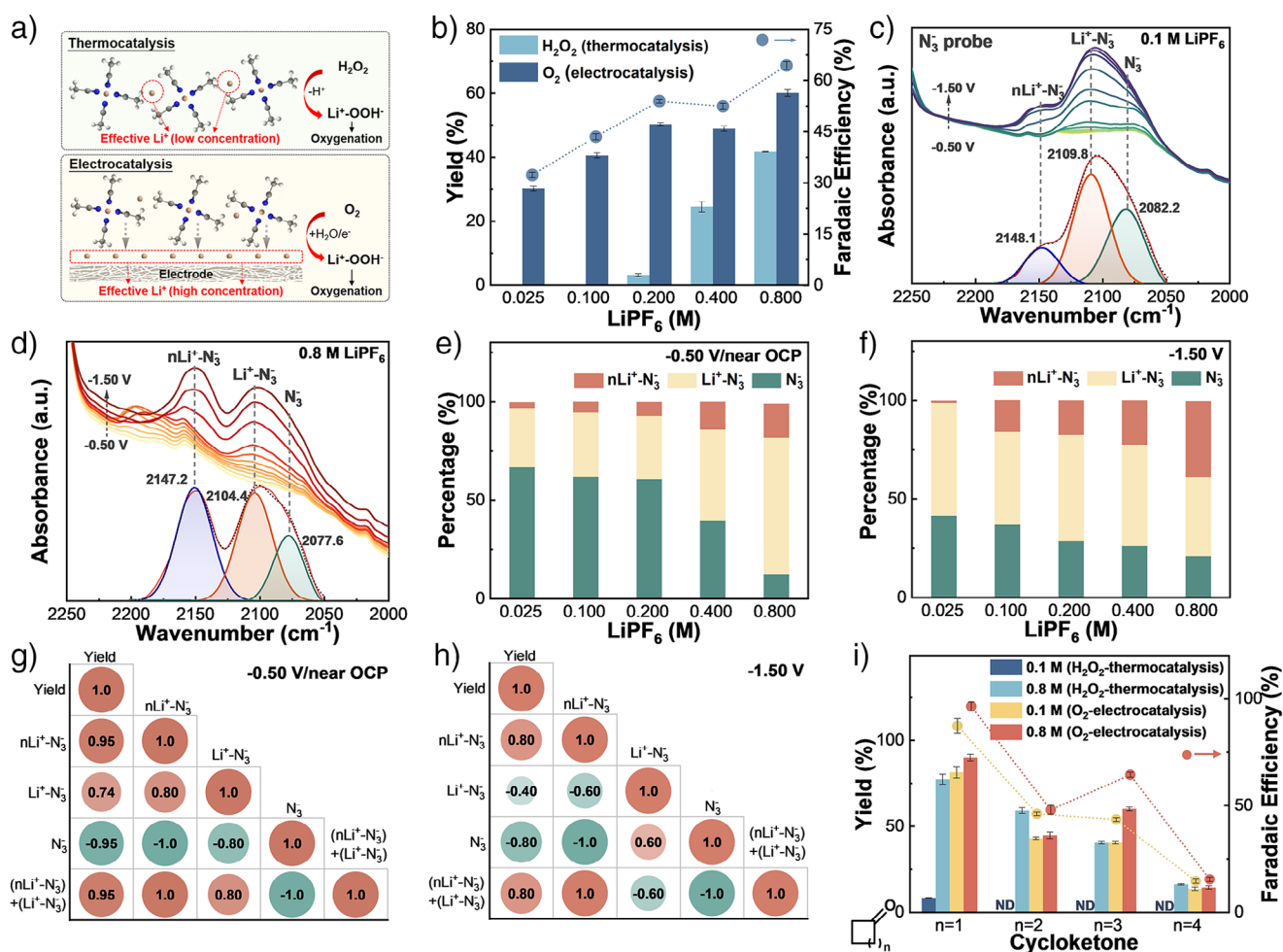


Figure 4. Quantitative description of interfacial Li^+ cations and their difference with bulk Li^+ cations. a) Schematic diagram of the effective Li^+ for the formation of $\text{Li}^+\text{-OOH}^-$ complexes toward oxygenation. b) The yield and Faradaic efficiency of $\varepsilon\text{-CL}$ in thermocatalytic/electrocatalytic scenarios with different LiPF_6 concentrations. Electrolysis conditions: 60 mM cyclohexanone, 0.025/0.1/0.2/0.4/0.8 M LiPF_6 , O_2 /60 mM H_2O_2 , 5 mL acetonitrile, room temperature, constant current density of 20 or 0 mA cm^{-2} for 2700 s. c) and d) The ATR-SEIRAS spectra of the system when polarized to different potentials in c) 0.1 M and d) 0.8 M LiPF_6 system with saturated N_3^- . The orange curve represents the background-removed spectrum and fitted spectra of the raw data of the -1.50 V versus Fc^+/Fc infrared spectrum. e) and f) The proportions of different forms of N_3^- and Li^+ -coordinated N_3^- in LiPF_6 systems with different concentrations e) near OCP and f) under -1.50 V versus Fc/Fc^+ . g) and h) Kendall correlation coefficient between different forms of N_3^- / Li^+ coordinated- N_3^- and $\varepsilon\text{-CL}$ yield g) near OCP and h) under -1.50 V versus Fc/Fc^+ . i) Yield and Faradaic efficiency of different products for the oxygenation of different cycloketones under both thermocatalytic/electrocatalytic scenarios. Electrolysis conditions: 60 mM ketone, 0.1/0.8 M LiPF_6 , O_2 /60 mM H_2O_2 , 5 mL acetonitrile, room temperature, constant current density of 0 or 20 mA cm^{-2} for 2700 s. The error bars correspond to the standard deviation of at least three independent measurements, and the center value for the error bars is the average of the three independent measurements.

consistent trend, but the exception is the thermocatalytic condition under LiTFSI . No product was detected even at very large concentrations. The LiTFSI can be readily solubilized because the Li^+ and TFSI^- facily formed $\text{Li}^+\text{-TFSI}^-$ ion pairs. These ion pairs bury the Li^+ and prevent the formation of active $\text{Li}^+\text{-OOH}^-$ complexes, while the applied electric field pulled away the ion pairs to construct the Li^+ -accumulated interface and allowed the formation of active $\text{Li}^+\text{-OOH}^-$ species. Overall, this strategy of utilizing interfacial anions to modulate the nature and concentration of active species is highly effective and also shines light on the intrinsic differences and similarities of chemoreactivity in electrocatalytic and thermocatalytic systems. This strategy and relevant analysis could be further extended to the

oxygenation of other ketone systems, especially the highly resembled activities of 0.1 M Li^+ /electrocatalysis and 0.8 M Li^+ /thermocatalysis, and can provide a reference for other ion-sensitive systems (Figure 4i).

Conclusion

Herein, by simulating the unique electrostatic interaction in BVMO enzymes, we discovered that the electrostatically enriched Li^+ cations can efficiently catalyze the aerobic oxygenation of ketones. Through systematic optimization, we demonstrated that the effective accumulation of Li^+ cations induced by the applied potential and carboxylated carbon

nanotube electrodes can generate a high yield of 60.1% and a Faradaic efficiency of 64.42% for the representative cyclohexanone oxidation. The enriched Li^+ cations can not only induce short-range electrostatic interactions with the OOH^- intermediate generated by the H_2O -involved O_2 electro-reduction but also attract excessive H_2O dipoles to prevent the annihilation of the active $\text{Li}^+\text{-OOH}^-$ complex. Kinetic analysis, in situ spectroscopy, and DFT calculations reveal that the side-on $\text{Li}^+\text{-OOH}^-$ complex can effectively reduce the energy barrier of O_2 reduction and increase the nucleophilicity toward oxygenation. The competition of the $\text{Li}^+\text{-OOH}^-$ complex with the proton source and anionic species was highly critical for the activity, which led to the concept of effective Li^+ at the interface that facilely forms the $\text{Li}^+\text{-OOH}^-$ complex. The effective Li^+ concentration behaves very differently at the electrode/electrolyte interface and in the bulk solution. This difference accounts for the observed distinction between electrocatalysis and thermocatalysis. By using the N_3^- probe-assisted method, we quantified the effective Li^+ fraction that can facilely form short-range electrostatic interactions with anionic species and revealed that the electrostatically enriched Li^+ cations are more effective than the bulk Li^+ cations for creating desired electrostatic interactions, by a factor of up to eight. This discrepancy shines light on the intrinsic chemoreactivity difference in electrocatalysis and thermocatalysis, and this work points to the prospective route of utilizing electrostatically enriched ions for the efficient catalytic transformation, especially toward the synthesis of fine chemicals.

Supporting Information

The authors have cited additional references within the Supporting Information.^[45–48]

Acknowledgements

This work was financially supported by the National Natural Science Foundation of China (Nos. 22172036, 21876049, 22222602, and 92477126) and the Shanghai Pujiang Program (21PJD016).

Conflict of Interests

The authors declare no conflict of interest.

Data Availability Statement

The data that support the findings of this study are available from the corresponding author upon reasonable request.

Keywords: Electrocatalysis • Electrostatic interaction • Interfacial ion • Oxygen reduction • Oxygenation

- [1] M. Y. Jin, Q. Zhen, D. Xiao, G. Tao, X. Xing, P. Yu, C. Xu, *Nat. Comm.* **2022**, *13*, 3276.
- [2] C. J. Laconsay, T. J. Seguin, S. E. Wheeler, *ACS Catal.* **2020**, *10*, 12292–12299.
- [3] R. Robiette, T. Trieu-Van, V. K. Aggarwal, J. N. Harvey, *J. Am. Chem. Soc.* **2016**, *138*, 734–737.
- [4] A. J. Neel, M. J. Hilton, M. S. Sigman, F. D. Toste, *Nature* **2017**, *543*, 637–646.
- [5] R. Maji, S. C. Mallojjala, S. E. Wheeler, *Acc. Chem. Res.* **2023**, *56*, 1990–2000.
- [6] J. Yi, S. Zhan, L. Chen, Q. Tian, N. Wang, J. Li, W. Xu, B. Zhang, M. S. Ahlquist, *J. Am. Chem. Soc.* **2021**, *143*, 2484–2490.
- [7] S. Zhan, B. Zhang, L. Sun, M. S. Ahlquist, *ACS Catal.* **2020**, *10*, 13364–13370.
- [8] Z. Huang, Y. Bai, X. Huang, J. Li, Y. Wu, Y. Chen, K. Li, X. Niu, N. Li, G. Liu, *Nature* **2023**, *623*, 531–537.
- [9] F. A. Perras, D. Marion, J. Boisbouvier, D. L. Bryce, M. J. Plevin, *Angew. Chem. Int. Ed.* **2017**, *129*, 7672–7675.
- [10] H. R. Kilgore, R. T. Raines, *J. Am. Chem. Soc.* **2018**, *140*, 17606–17611.
- [11] E. D. Getzoff, J. A. Tainer, P. K. Weiner, P. A. Kollman, J. S. Richardson, D. C. Richardson, *Nature* **1983**, *306*, 287–290.
- [12] T. A. Coulther, J. Ko, M. J. Ondrechen, *J. Chem. Phys.* **2021**, *154*, 195101.
- [13] S. J. Benkovic, S. Hammes-Schiffer, *Science* **2003**, *301*, 1196–1202.
- [14] D. K. Romney, S. M. Colvin, S. J. Miller, *J. Am. Chem. Soc.* **2014**, *136*, 14019–14022.
- [15] J. H. Maalouf, K. Jin, D. Yang, A. M. Limaye, K. Manthiram, *ACS Catal.* **2020**, *10*, 5750–5756.
- [16] Q. Ma, W. Xing, J. Xu, X. Peng, *Catal. Comm.* **2014**, *53*, 5–8.
- [17] M. J. Fürst, A. Gran-Scheuch, F. S. Aalbers, M. W. Fraaije, *ACS Catal.* **2019**, *9*, 11207–11241.
- [18] A. Corma, L. T. Nemeth, M. Renz, S. Valencia, *Nature* **2001**, *412*, 423–425.
- [19] M. J. Fürst, S. Savino, H. M. Dudek, J. R. b. Gómez Castellanos, C. Gutiérrez de Souza, S. Rovida, M. W. Fraaije, A. Mattevi, *J. Am. Chem. Soc.* **2016**, *139*, 627–630.
- [20] B. J. Yachnin, T. Sprules, M. B. McEvoy, P. C. Lau, A. M. Berghuis, *J. Am. Chem. Soc.* **2012**, *134*, 7788–7795.
- [21] C. J. Hastings, M. D. Pluth, R. G. Bergman, K. N. Raymond, *J. Am. Chem. Soc.* **2010**, *132*, 6938–6940.
- [22] X. Ren, M. Guo, H. Li, C. Li, L. Yu, J. Liu, Q. Yang, *Angew. Chem. Int. Ed.* **2019**, *58*, 14483–14488.
- [23] X. Li, L. Liu, X. Ren, J. Gao, Y. Huang, B. Liu, *Sci. Adv.* **2020**, *6*, eabb6833.
- [24] H. Zou, S. Shu, W. Yang, Y.-c. Chu, M. Cheng, H. Dong, H. Liu, F. Li, J. Hu, Z. Wang, *Nat. Commun.* **2024**, *15*, 10818.
- [25] Y. Min, S.-C. Mei, X.-Q. Pan, J.-J. Chen, H.-Q. Yu, Y. Xiong, *Nat. Commun.* **2023**, *14*, 5134.
- [26] X. Y. Li, T. Wang, Y. C. Cai, Z. D. Meng, J. W. Nan, J. Y. Ye, J. Yi, D. P. Zhan, N. Tian, Z. Y. Zhou, *Angew. Chem. Int. Ed.* **2023**, *62*, e202218669.
- [27] X. Yang, H. Ding, S. Li, S. Zheng, J.-F. Li, F. Pan, *J. Am. Chem. Soc.* **2024**, *146*, 5523–5542.
- [28] X. Qin, H. A. Hansen, K. Honkala, M. M. Melander, *Nat. Comm.* **2023**, *14*, 7607.
- [29] M. A. Gebbie, B. Liu, W. Guo, S. R. Anderson, S. G. Johnstone, *ACS Catal.* **2023**, *13*, 16222–16239.
- [30] Y. Mu, B. Chen, H. Zhang, M. Fei, T. Liu, N. Mehta, D. Z. Wang, A. J. Miller, P. L. Diaconescu, D. Wang, *J. Am. Chem. Soc.* **2024**, *146*, 13438–13444.
- [31] X. Luo, Y. Wang, B. Wu, Y. Wang, C. Li, M. Shao, B. Liu, Z. Wei, *J. Phys. Chem. Lett.* **2024**, *15*, 10435–10441.

- [32] L. Gong, J. Zhu, F. Xia, Y. Zhang, W. Shi, L. Chen, J. Yu, J. Wu, S. Mu, *ACS Catal.* **2023**, *13*, 4012–4020.
- [33] C. Zhang, W. Shen, K. Guo, M. Xiong, J. Zhang, X. Lu, *J. Am. Chem. Soc.* **2023**, *145*, 11589–11598.
- [34] Y. Bu, Y. Wang, G. F. Han, Y. Zhao, X. Ge, F. Li, Z. Zhang, Q. Zhong, J. B. Baek, *Adv. Mater.* **2021**, *33*, 2103266.
- [35] J. S. Lim, J. H. Kim, J. Woo, D. San Baek, K. Ihm, T. J. Shin, Y. J. Sa, S. H. Joo, *Chem* **2021**, *7*, 3114–3130.
- [36] I. M. AlNashef, M. L. Leonard, M. C. Kittle, M. A. Matthews, J. W. Weidner, *Electrochem. Solid-State Lett.* **2001**, *4*, D16.
- [37] Y. Zhang, X. Zhang, J. Wang, W. C. McKee, Y. Xu, Z. Peng, *J. Phys. Chem. C* **2016**, *120*, 3690–3698.
- [38] Z. Peng, Y. Chen, P. G. Bruce, Y. Xu, *Angew. Chem. Int. Ed.* **2015**, *127*, 8283–8286.
- [39] Z. Jiang, A. M. Rappe, *J. Am. Chem. Soc.* **2022**, *144*, 22150–22158.
- [40] J. Chlistunoff, J.-P. Simonin, *J. Phys. Chem. A* **2006**, *110*, 13868–13876.
- [41] R. Pino-Rios, D. Inostroza, G. Cárdenas-Jirón, W. Tiznado, *J. Phys. Chem. A* **2019**, *123*, 10556–10562.
- [42] T. Kumeda, L. Laverdure, K. Honkala, M. M. Melander, K. Sakaushi, *Angew. Chem. Int. Ed.* **2023**, *135*, e202312841.
- [43] X. Chen, Q. Zhang, *Acc. Chem. Res.* **2020**, *53*, 1992–2002.
- [44] X. Chen, X. Q. Zhang, H. R. Li, Q. Zhang, *Batteries Supercaps* **2019**, *2*, 128–131.
- [45] Z. Lu, G. Chen, S. Siahrostami, Z. Chen, K. Liu, J. Xie, L. Liao, T. Wu, D. Lin, Y. Liu, *Nat. Catal.* **2018**, *1*, 156–162.
- [46] J. Moellmann, S. Grimme, *J. Phys. Chem. C* **2014**, *118*, 7615–7621.
- [47] A. P. Scott, L. Radom, *J. Phys. Chem. C* **1996**, *100*, 16502–16513.
- [48] T. Lu, F. Chen, *J. Comput. Chem.* **2012**, *33*, 580–592.

Manuscript received: January 07, 2025

Revised manuscript received: March 25, 2025

Accepted manuscript online: April 01, 2025

Version of record online: April 10, 2025